

See discussions, stats, and author profiles for this publication at: <https://www.researchgate.net/publication/257816152>

In situ electrochemical X-ray spectromicroscopy investigation of the reduction/reoxidation dynamics of Ni-Cu solid oxide fuel cell anodic material in contact with a Cr interconnect

ARTICLE *in* THE JOURNAL OF PHYSICAL CHEMISTRY C · JANUARY 2012

Impact Factor: 4.77

CITATIONS

2

READS

37

1 AUTHOR:



[Maya Kiskinova](#)

Sincrotrone Trieste S.C.p.A.

82 PUBLICATIONS 725 CITATIONS

[SEE PROFILE](#)

In Situ Electrochemical X-ray Spectromicroscopy Investigation of the Reduction/Reoxidation Dynamics of Ni–Cu Solid Oxide Fuel Cell Anodic Material in Contact with a Cr Interconnect in 2×10^{-6} mbar O₂

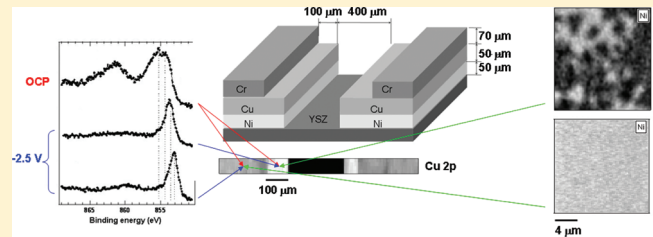
Benedetto Bozzini,^{*,†} Matteo Amati,[‡] Luca Gregoratti,[‡] Majid Kazemian,[‡] Mauro Prasciolu,[§] Elisabetta Tondo,[†] Alexander L. Trygub,[‡] and Maya Kiskinova[‡]

[†]Dipartimento di Ingegneria dell'Innovazione, Università del Salento, via Monteroni s.n., 73100 Lecce, Italy

[‡]Sincrotrone Trieste S.C.p.A., ELETTRA, S.S. 14 km 163.5 in Area Science Park, 34012 Basovizza, Trieste, Italy

[§]CNR-INFM TASC National Laboratory, S.S. 14, km 163.5 in Area Science Park, 34012 Trieste-Basovizza, Italy

ABSTRACT: Following our systematic investigations on the durability of solid oxide fuel cell (SOFC) components (Bozzini, B.; Tondo, E.; Prasciolu, M.; Amati, M.; Kazemian, M.; Gregoratti, L.; Kiskinova, M. *ChemSusChem*, <http://dx.doi.org/10.1002/cssc.201100140>), the present in situ scanning photoelectron microscopy study is focused on the redox behavior of Ni–Cu bilayers in contact with Cr, representing the anodic material and interconnects for SOFCs, respectively. The experiments with this model cell, using yttria-stabilized zirconia (YSZ) electrolyte, were carried out in 2×10^{-6} mbar O₂ at 650 °C at open circuit potential (OCP) and under applied potential. The elemental images and the spectra from selected parts of the cell have revealed dramatic compositional and morphological changes under OCP conditions, yielding Ni–Cu islands covered with NiO in the electrode region and a NiO network in the YSZ electrolyte region. The Ni reduction dynamics as a function of applied potential is followed by continuous monitoring of the evolution of the Ni 2p spectra in different regions, which allowed the location of electrochemically active areas of the half-cell upon cathodic polarization. It was shown that after electrochemical reduction the reoxidation at OCP results in notable morphology alterations of the triple-phase contact region, which can be related to the empirically observed degradation of catalytic performance.



1. INTRODUCTION

Conventional anodic systems for solid oxide fuel cells (SOFCs) operating on both traditional and innovative fuels (hydrogen and hydrocarbons, respectively) are manufactured from Ni-based compounds, in combination with a dispersed solid electrolyte (typically YSZ) or mixed ionic–electronic conductors (e.g., Ce(III)/Ce(IV) oxides), in order to enhance the density of the three-phase boundaries (TPB).^{2–4} Ni is used for its excellent conductivity and catalytic activity. Moreover, Ni cermets are relatively simple to fabricate: in particular, it is possible to sinter NiO–YSZ composites and then to reduce them to form a Ni–YSZ cermet in the environment of a fuel cell anode.⁵ The use of hydrocarbons in SOFCs^{5,6} yields specific durability problems of Ni-based catalysts; most common are poisoning by sulfides (present in the fuel), which blocks the active sites, and deactivation by carbon buildup;⁷ for these reasons alternative materials are being sought for anodes. Cu is a promising alternative owing to its good catalytic activity, high conductivity, and coefficient of thermal expansion compatible with other components of the cell.^{8,9} The use of Ni–Cu alloys is even more attractive because

they offer both the catalytic enhancement of Ni and the stabilizing effect of Cu by reducing carbon formation.¹⁰

Another important source of catalyst degradation is anode reoxidation resulting from transient exposure of anodic material to air or oxygen, a rather common event during cell operation.¹¹ In fact, the release of oxygen during the conversion of NiO to Ni typically leads to the formation of a high density of micropores: such morphology changes affect the anode electrochemical activity, which crucially depends on the density of triple-phase boundary, consisting of Ni grains, electrolyte grains, and gas-containing pores.¹² Cyclic reduction and reoxidation of NiO-based anodes emphasizes this problem, causing structural changes that not only deteriorate the catalytic performance¹³ but also lead to cracking of cell components.^{11,14} The effect of reduction and reoxidation cycling on catalytic performance of anode materials has been the object of many studies, chiefly using temperature-programmed measurements and carried out in the relevant reactive environments.^{15–18} The

Received: September 2, 2011

Revised: December 22, 2011

Published: March 7, 2012

present understanding indicates as important factors the electrode composition, the preparation technique,¹⁶ and the operating parameters.¹⁴ Apart from catalyst degradation, another critical durability problem of SOFCs is the corrosion of interconnects. In SOFCs operating at intermediate temperatures (600–800 °C), the interconnects material of choice is ferritic stainless steel, essentially for its low cost compared to the traditional ceramic materials;^{19,20} furthermore, these stainless grades have a thermal expansion coefficient that matches well the other fuel cell stack components.²¹ However, the use of stainless steel is not devoid of drawbacks since its high Cr content leads to the formation of volatile Cr-based compounds that poison the cell, deteriorating its performance. Apparently, shedding light on the reoxidation-induced anode and interconnect degradation mechanisms requires *in situ* monitoring of processes occurring in the cell components under electrochemical operating conditions.

The present *in situ* scanning photoelectron microscopy (SPEM) study of SOFC degradation mechanisms is focused on the early stages of reduction of preoxidized Cu–Ni bilayers: a model catalyst system for hydrocarbon anodes. Exposures to O₂ environment at high temperature reproduce the as-fabricated conditions, and subsequent cathodic polarization follows the evolution of the anodic material by controlling electrochemically the reducing potential. Furthermore, the Cu–Ni bilayer is in contact with a Cr layer, which adds information about the processes occurring at the anode/interconnects interface. Thanks to the combination of chemical imaging and microspectroscopy with submicrometer spatial resolution, this model system approach is liable to yield unprecedented mechanistic information on both reduction and reoxidation processes under electrochemical control in the reactive gas environment with running faradaic reactions.

2. EXPERIMENTAL METHODS

2.1. Cell Fabrication and Electrochemical Testing Conditions.

In order to perform *in situ* electrochemical SPEM measurements under controlled gas ambient, temperature, and potential conditions, we fabricated lithographically a cell containing the chief components of the anodic half-cell, based on the design proposed and described in detail in a previous publication of ours.²² The planar-cell geometry and the arrangement of the thin film electrodes are depicted in Figure 1a. In the Cr/Cu–Ni/YSZ/Ni–Cu/Cr stack, Cr represents the Cr-containing interconnect, Cu–Ni the catalyst, and YSZ the electrolyte. Each Cr/Cu–Ni trilayer was connected to a potentiostat either as a working electrode (WE) or simultaneously as a reference- (RE) and counter- (CE) electrode. Thus the voltages reported in the text have to be meant as cell potentials. Notwithstanding the electrode material evolution described in sections 3.2 and 3.3, the asymptotic OCP values obtained with both electrodes in their oxidized form were highly reproducible and values in the range 0 ± 8 mV were measured. The potentials refer to the cell bias and the possible electrodic reactions are (i) reduction of O₂ and metal oxides at the cathode and (ii) oxidation of O²⁻ species and metals at the anode. The focus of this investigation is on the anodic half-cell.

For *in situ* electrochemical experiments, the electrochemical cell was placed inside the SPEM chamber and run in O₂ ambient of 2 × 10⁻⁶ mbar. Both electrodes of the cell are connected with Pt clips to the sample holder floating contacts which through Cu shielded cables and feedthroughs bring the

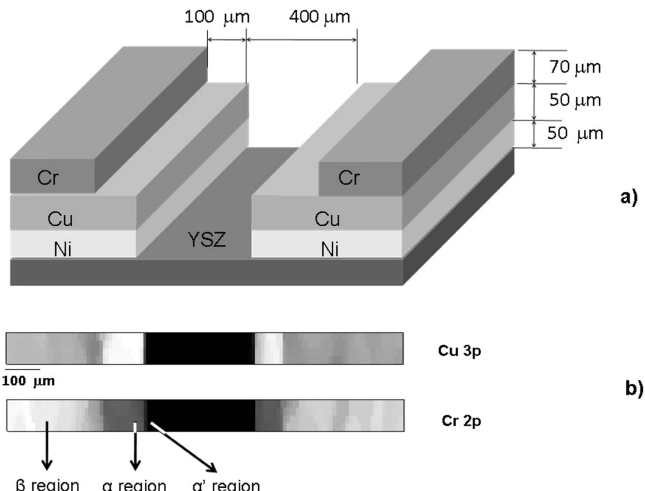


Figure 1. (a) Scheme of the planar electrochemical cell for *in situ* SPEM measurements under electrochemical control. (b) Cu 2p and Cr 2p SPEM images of the pristine cell recorded at room temperature in UHV.

electrical connections to the air-side of the vacuum chamber. The planar cell was put in contact with a boron-nitrate-encapsulated commercial heater capable of reaching high temperature in oxidizing conditions without damaging. The temperature was raised to 650 °C at OCP, and subsequently the evolution of the Cr/Cu–Ni trilayers was examined under controlled electrochemical polarization.

2.2. In Situ SPEM Measurements. All measurements were carried out in the SPEM station of the ESCAmicroscopy beamline at the ELETTRA synchrotron in Trieste, Italy. The SPEM operates in imaging and spectroscopic modes using X-ray nanoprobe provided by Fresnel zone plate. Using the imaging mode, we monitored the lateral distribution of the electrodes and electrolyte element constituents by collecting the photoelectrons emitted within the selected atomic core level energy window (Ni 2p, Cu 2p, Cr 2p, and Zr 3d in our case) while raster scanning the specimen with respect to the nanoprobe. The spatial variation in the image contrast reflects the variation of the photoelectron yield, which is a measure of the local concentration of the given element. The microspot spectroscopy mode is identical to conventional XPS and provides all details about the chemical states of the elements present in the selected spot of the size of the focused beam. The present studies were carried out with photon energy 1050 eV, nanoprobe of 120 nm, and 0.2 eV spectral resolution. More details about SPEM and the beamline are given in refs 23 and 24.

3. RESULTS AND DISCUSSION

3.1. Evolution of SOFC Components under OCP Conditions.

In this section we report the SPEM results obtained when the as-fabricated cell is exposed to 2 × 10⁻⁶ mbar O₂ and heated to the working temperature of 650 °C, called OCP conditions. The Cr 2p and Cu 2p maps of the as-fabricated cell in Figure 1b show that CuNi bilayer and CrCuNi trilayer patches can be easily distinguished so the evolution of the composition and morphology of each patch, represented by the locations denoted as α and β , can be monitored on a local scale. The Ni 2p and Cu 2p spectra in Figure 2 measured at OCP upon stepwise heating in 2 × 10⁻⁶ mbar O₂ until reaching the target temperature of 650 °C illustrate the evolution of the

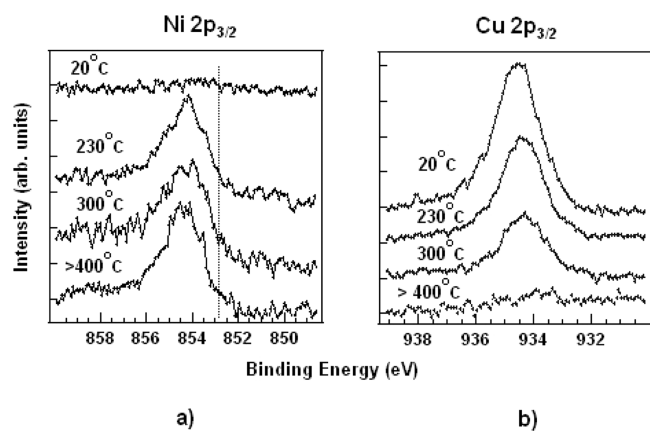


Figure 2. Ni 2p and Cu 2p spectra measured in region α starting from a pristine cell at room temperature and stepwise increasing the temperature to 650 °C in 10^{-6} mbar O₂. The spectra are measured 30 min after reaching the indicated temperature. The changes observed in the Cu 2p region are irreversible as notified in the text. The dashed line in the Ni 2p panel indicates the position of metallic Ni component.

surface composition and chemical state of the CuNi bilayer (α in Figure 1). The spectra show that initially (UHV, 20 °C) Ni, being below the Cu layer, is hardly detectable in the Ni 2p spectra, whereas Ni spectral features corresponding to Ni oxide state appear and grow upon exposing to oxygen ambient and increasing the temperature. The Cu 2p spectra, instead, progressively lose intensity and cannot be recovered with successive application of either reducing (section 3.2) or reoxidizing (section 3.3) conditions. This result is a clear evidence of Ni oxide segregation on the surface, concomitant with the higher affinity of Ni to oxygen which is the thermodynamic driving force for Ni segregation. From estimation of the probing depth under our experimental conditions, the complete damping of the Cu 2p emission

indicates that the thickness of the Ni oxide layer should be ≥ 2 nm. As reported below, the Ni 2p spectrum corresponds to stoichiometric NiO with a broad main peak centered at 855 eV, and the typical intense satellite structure shifted by 6 eV²⁵ is fully developed after longer exposures reaching the steady conditions.

The elemental maps and microspot spectra in Figure 3 summarize the final morphology and the chemical states achieved in the bilayer α and trilayer β regions after exposure to 2×10^{-6} mbar O₂ at 650 °C for 7 h, preceded by 2 h exposure to 2×10^{-6} mbar O₂ during ramping the temperature from 20 to 650 °C. The contrast variations in the Ni 2p maps taken in α reveal that the Ni oxide segregation is accompanied by the development of a complex morphology, where the contrast level indicates fractioning of the Ni–Cu layered structure, initially appearing uniform and continuous at our length scales. It should be noted that the stress in metal films induced by oxidation at high temperature can lead to development of a pore microstructure, possibly due to recrystallization and delamination of the film.^{26,27} This dramatic restructuring of the Cu–Ni film is confirmed by the appearance of an electron emission signal from the underlying YSZ electrolyte. The darker and brighter regions of the Ni maps indicate formation of microislands of variable thicknesses and pores, confirmed by inverse contrast of the Zr 3d and Ni 2p maps in Figure 3. Since the Ni 2p and Zr 3d signals can be detected in both darker and brighter regions of the maps reported in Figure 3a, b, these regions should be considered as Ni-rich and Ni-poor, most likely with a nanocluster-type morphology. Consequently, the extinction of the Cu signal should be tentatively attributed to the formation of core–shell type islands; i.e., the nickel, diffusing most likely via grain boundaries, covers the pieces of disrupted Cu film with a 2–3 nm Ni oxide shell, sufficient to damp the emission from the Cu core. The formation of a connected network of NiO enclosing areas of YSZ provides an optimal triple-phase contact: this region of the electrode turns

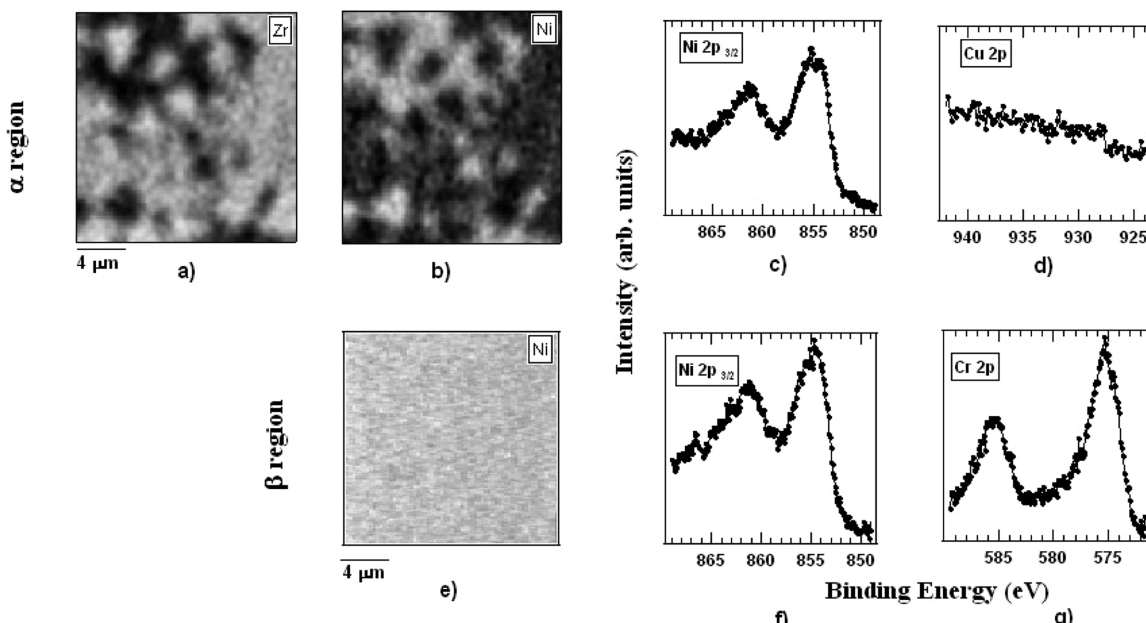


Figure 3. (a, b) Zr 3d and Ni 2p maps of NiCu region α . (c, d) Ni 2p and Cu 2p micro-XPS for location α . (e) Ni 2p map of NiCuCr region β . (f, g) Ni 2p and Cr 2p micro-XPS for region β . All measurements were performed in 2×10^{-6} mbar O₂ at 650 °C under OCP conditions after attainment of steady-state conditions (ca. 7 h).

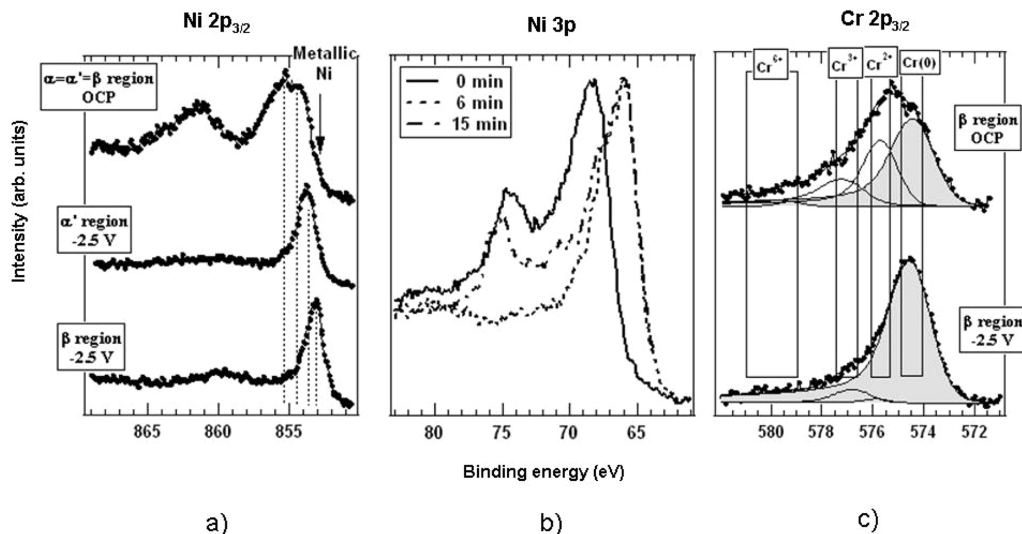


Figure 4. Ni 2p and Cr 3p micro-XPS measured in the indicated regions of Figure 1b in 2×10^{-6} mbar O₂ at 650 °C under the indicated electrochemical conditions. (a) and (c) report steady-state conditions (upper spectra, ca. 7 h of exposure to O₂; middle and bottom spectra after more than 30 min with applied potential); (b) shows a typical reduction transient for Ni at -2.5 V.

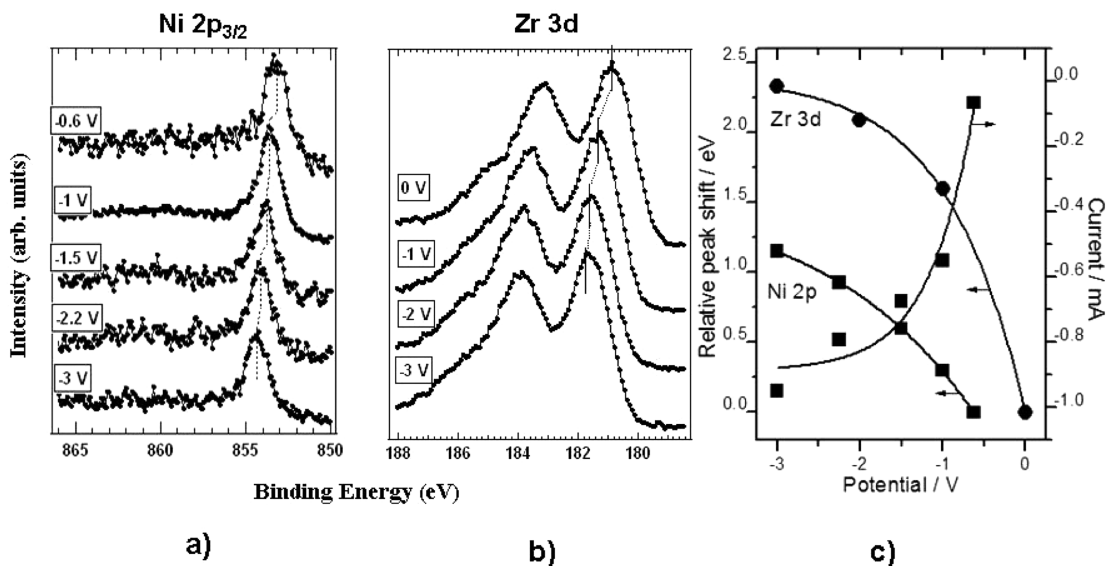


Figure 5. Ni 2p_{3/2} (panel a, location α') and Zr 3d (panel b, center of the electrolyte) micro-XPS spectra recorded during application of the cathodic polarization at the indicated potentials. Data measured in 2×10^{-6} mbar O₂ at 650 °C. (c) Relative peak shifts and cell current as a function of applied cell voltage. The spectra of panel a have been acquired sequentially after having attained steady state conditions at -0.6 V (ca. 1 h with applied potential). The spectra of panel b have been measured after the cell had been held at OCP for ca. 10 h. The scatter plots refer to experimental data, the black line is a guide for the eye, the blue line is a fit with a general model for electrochemical kinetics with mixed control.³³

out to be the most electrochemically active in our half-cell, as reported in section 3.2.

The evolution of the region β , located deep inside the Cr patch, is very different. The observed Ni diffusion onto the Cr patch is coherent with our previous findings.¹ However, the acquired spectra denote only the presence of Ni and Cr, without any trace of Cu and Zr. The Ni 2p map of this region, shown in Figure 3e, has uniform contrast level confirming that the film has preserved its pristine continuity. This indicates that the Cr film has a stabilizing role and the out-diffusion of Ni does not lead to disruption of the Ni–Cu–Cr trilayer. The line shape and presence of strong oxide-related plasmon feature in Ni 2p spectra show that the Ni species, uniformly spread onto the Cr patch, are fully oxidized. More details about the Cr chemical state are provided by the top Cr 2p spectra in Figure

4b, where the components of Cr 2p deconvolution show coexistence of Cr species in different oxidation states.²⁸ However, the presence of a strong metallic component indicates that the Cr oxide thickness does not exceed 1–2 nm.

3.2. Evolution of SOFC Components under Reducing Conditions. The processes occurring under reducing conditions, by imposing different levels of cathodic polarization at one of the electrodes, are examined in the three representative locations indicated in Figure 1: α and β and α' (at the Ni/YSZ interface). As shown in some recent papers,^{4,29,30} such experiments allow an accurate identification of the electrochemically active region of the half-cell and of the local electrokinetics. The Ni 2p and Cr 2p spectra in panels a and b of Figure 4, measured after reaching the steady state upon applying -2.5 eV for 30 min, clearly manifest that both Ni and

Cr oxides undergo reduction. Few sequential Ni 2p spectra, illustrating time-dependent reduction of Ni oxide at -2.5 V, are shown in panel c, and more information on the time dependence of in situ electrochemical reduction is reported in a previous paper.¹ It is worth noting that the time required for complete reduction decreases with increasing potential, e.g., for NiO ca. 15 min at -1 V and ca. 6 min at -2.5 eV. However, close inspection of the Ni 2p spectra shows that starting from the same oxidation state at OCP the Ni 2p spectra of the reduced state are slightly shifted with respect to that measured in position β . This shift as a function of the location under applied electrochemical potential is due to overvoltage distribution along the planar electrode. In principle, this overvoltage distribution can be due to ohmic, charge-transfer, and mass-transport contributions: the first can be related to changes in electrode thickness due to the formation of islands, the second one to the localization of electrochemical reactions at the electrode–electrolyte interface, and the last one to surface diffusion of electroactive species. In this case zone α' , being closer to the O_2 /electronic conductor (Ni/NiO)/electrolyte (YSZ) triple-phase boundary, is more electrochemically active and shows both a higher charge-transfer overvoltage and more evident formation of TPBs. This result is corroborated with the evolution of the spectra reported in Figure 5a, measured in the electrochemically active region α' at different cathodic potentials. The observed systematic decrease of Ni 2p photoelectron kinetic energy (Figure 5a) correlates with the increase of the applied potential and the corresponding overvoltage. Such nonlinearity can be attributed to predominance of charge-transfer and mass-transport contributions, coherently with the current–voltage behavior reported in the inset, where the peak shifts for the reduced state and the corresponding currents obtained by scanning the potential from OCP to -3.0 V are compared. Results, similar to our in situ SPEM direct measurement of the localization of electrochemical overvoltages, have recently been reported for different systems: ceria electrodes^{4,29} and a Ni electrode.³⁰ As a consistency check, we also recorded the Zr 3d spectra from the electrolyte in the central part of the cell. Since no electrochemical reactions occur in this region, the local potential is a result of the reaction overvoltages of the two electrodes and of the ohmic drop within the electrolyte, confirmed by the observed peak shift and its nonlinearity with respect to the applied cell voltage.

3.3. Evolution of SOFC Components upon Reoxidation at OCP. After electrochemical reduction of the working electrode, we monitored its reoxidation by exposure to O_2 for 7 h at OCP. The morphology changes after applying reducing cathodic conditions and following reoxidation cycles are summarized in Figure 6. The images evidence that the highly catalytically active network pore structure, giving access to YSZ, is somewhat preserved after reduction, but further restructuring is taking place upon reoxidation and the film expands beyond the initial boundaries that have apparently smeared. The oxidation process—though predictable on the basis of the results reported in section 3.1—has been confirmed by the presence of oxide state features in the Ni and Cr 2p spectra measured in different cell locations that are identical to those shown in Figures 3 and 4. Our in situ reoxidation results yield direct evidence for the irreversible structural changes of Ni-based substrates confirming the previously reported ex situ measurements;^{11,31,32} this phenomenon has to be responsible

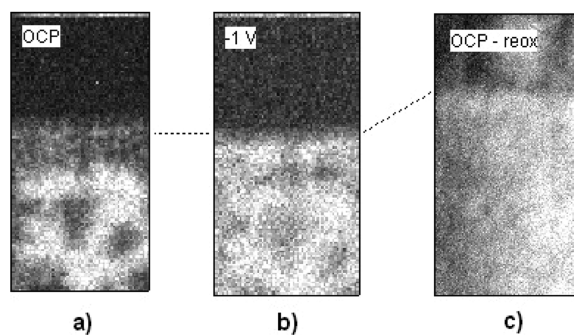


Figure 6. SPEM images (Ni 2p energy) of the Ni/YSZ interface of the working electrode, measured in the following conditions: (a) oxidized at OCP (ca. 7 h), (b) reduced at -1 V (ca. 4 h), (c) reoxidized at OCP (ca. 7 h). All measurements were carried out in 2×10^{-6} mbar O_2 at 650 °C. The position of the Ni/YSZ interface has been indicated by a dashed line.

for the changes in anode activity with electrochemical cycling between reducing and oxidizing conditions.

4. CONCLUSIONS

The present in situ scanning photoelectron microscopy study of model electrochemical cell working at 650 °C in O_2 ambient is shedding light on reduction and reoxidation dynamics of the anodic Ni–Cu materials for hydrocarbon-fueled SOFCs and the degradation processes of the metal (Cr) interconnects. It has been shown that the initial Ni–Cu bilayer undergoes dramatic changes in oxidative environment at OCP: progressive segregation of Ni layer on top the Cu surface, accompanied by formation of metal oxides and dramatic structural changes. These processes result in formation of NiO-shell/Cu-core type humps, a new electrode morphology that provides an optimal triple-phase boundary structure. Ni also spreads over the Cr interconnect region, but without inducing visible morphology changes in this area. Progressive reduction of NiO to metallic Ni has been assessed upon application of cathodic polarization, and the electrochemically active region has been determined with nanometric precision by the apparent position-dependent Ni 2p binding energy shifts. Subsequent reoxidation of the electrochemically reduced material at OCP confirms that the developed new morphology can be correlated with the electrode degradation processes reported for operating SOFCs that have undergone reoxidation events.

■ AUTHOR INFORMATION

Corresponding Author

*Telephone +39-0832-297323, fax +39-0832-297733, e-mail benedetto.bozzini@unisalento.it.

■ REFERENCES

- (1) Bozzini, B.; Tondo, E.; Prasciolu, M.; Amati, M.; Kazemian, M.; Gregoratti, L.; Kiskinova, M. *ChemSusChem*, <http://dx.doi.org/10.1002/cssc.201100140>.
- (2) Badwal, S. P. S.; Fogar, K. *Ceram. Int.* **1996**, *22*, 257–265.
- (3) Zhu, W. Z.; Deevi, S. C. *Mater. Sci. Eng., A* **2003**, *362*, 228–239.
- (4) Zhang, C.; et al. *Nat. Mater.* **2010**, *9*, 944–949.
- (5) McIntosh, S.; Gorte, R. *Chem. Rev.* **2004**, *104*, 4845–4865.
- (6) Atkinson, A.; Barnett, S.; Gorte, R. J.; Irvine, J. T. S.; McEvoy, A. J.; Mogensen, M.; Singhal, S. C.; Vohs, J. *Nat. Mater.* **2004**, *3*, 17–27.
- (7) Yang, L.; Wang, S.; Liu, M.; Liu, Z.; Cheng, Z.; Liu, M. *Science* **2009**, *326*, 126–129.

- (8) Dongare, M. K.; Dongare, A. M.; Tare, V. B.; Kemnitz, E. *Solid State Ionics* **2002**, *152–153*, 455–462.
- (9) Gorte, R. J.; Vohs, J. M. *J. Catal.* **2003**, *216*, 477–486.
- (10) Kim, H.; Lu, C.; Worrell, W. L.; Vohs, J. M.; Gorte, R. J. *J. Electrochem. Soc.* **2002**, *149*, A247–A250.
- (11) Ettler, M.; Timmermann, H.; Malzbender, J.; Weber, A.; Menzler, N. H. *J. Power Sources* **2010**, *195*, 5452–5467.
- (12) Fukui, T.; Murata, K.; Ohara, S.; Abec, H.; Naito, M.; Nogi, K. *J. Power Sources* **2004**, *125*, 17–21.
- (13) Radovic, M.; Lara-Curzio, E. *Acta Mater.* **2004**, *52*, 5747–5756.
- (14) Blum, L.; et al. *Fuel Cells* **2007**, *7*, 204–210.
- (15) Baker, R. T.; Metcalfe, I. S. *Ind. Eng. Chem. Res.* **1995**, *34*, 1558–1565.
- (16) Mori, H.; Wen, C.; Otomo, J.; Eguchi, K.; Takahashi, H. *Appl. Catal., A* **2003**, *245*, 79–85.
- (17) Zhang, Y.; Liu, B.; Tu, B.; Dong, Y.; Cheng, M. *Solid State Ionics* **2009**, *180*, 1580–1586.
- (18) Su, C.; Wu, Y.; Wang, W.; Zheng, Y.; Ran, R.; Shao, Z. *J. Power Sources* **2010**, *195*, 1333–1343.
- (19) Zhu, W. Z.; Deevi, S. C. *Mater. Sci. Eng., A* **2003**, *348*, 227–243.
- (20) Lacey, R.; Pramanick, A.; Lee, J. C.; Jung, J.-I.; Jiang, B.; Edwards, D. D.; Naum, R.; Misture, S. T. *Solid State Ionics* **2010**, *181*, 1294–1302.
- (21) Chen, L.; Yang, Z.; Jha, B.; Xia, G.; Stevenson, J. W. *J. Power Sources* **2005**, *152*, 40–45.
- (22) Bozzini, B.; D'Urzo, L.; Gianoncelli, A.; Kaulich, B.; Prasciolu, M.; Sgura, I.; Tondo, E.; Kiskinova, M. *J. Phys. Chem. C* **2009**, *113*, 9783–9787.
- (23) Gregoratti, L.; Barinov, A.; Benfatto, E.; Cautero, G.; Fava, C.; Lacovig, P.; Lonza, D.; Kiskinova, M.; Tommasini, R.; Mahl, S. *Rev. Sci. Instrum.* **2004**, *75*, 64–69.
- (24) <http://www.elettra.trieste.it/experiments/beamlines/esca/index.html>.
- (25) Grosvenor, A. P.; Biesinger, M. C.; Smart, R. St. C.; McIntyre, N. S. *Surf. Sci.* **2006**, *600*, 1771–1779.
- (26) Kwon, Y.; Kim, N.-H.; Choi, G.-P.; Lee, W.-S.; Seo, Y.-J.; Park, J. *Microelectron. Eng.* **2005**, *82*, 314.
- (27) Kemdehoungja, C.; Grosseau-Poussart, J. L.; Dinhut, J. F.; Panicaud, B. *Matér. Techniq.* **2011**, *99*, 135–140.
- (28) Hassel, M.; Hemmerich, I.; Kuhlenbeck, H.; Freund, H.-J. *Surf. Sci. Spectr.* **1997**, *4*, 246–252.
- (29) DeCaluwe, S. C.; et al. *J. Phys. Chem. C* **2010**, *114*, 19853–19861.
- (30) El Gabaly, F.; Grass, M.; McDaniel, A. H.; Farrow, R. L.; Linne, M. A.; Hussain, Z.; Bluhm, H.; Liu, Z.; McCarty, K. F. *Phys. Chem. Chem. Phys.* **2010**, *12*, 12138–12145.
- (31) Waldbillig, D.; Wood, A.; Ivey, D. G. *J. Power Sources* **2005**, *145*, 206–215.
- (32) Klemens, T.; Mogensen, M. *J. Am. Ceram. Soc.* **2007**, *90*, 3582–3588.
- (33) Bozzini, B. *J. Chem. Educ.* **2000**, *77*, 100–103.